

Rapid Sensing of Hidden Objects and Defects using a Single-Pixel Diffractive Terahertz Processor

Jingxi Li^{1,2,3}, Xurong Li^{1,3}, Nezih T. Yardimci^{1,3}, Jingtian Hu^{1,2,3}, Yuhang Li^{1,2,3}, Junjie Chen⁴,
Yi-Chun Hung¹, Mona Jarrahi^{1,3}, and Aydogan Ozcan^{1,2,3*}

¹Electrical and Computer Engineering Department, University of California, Los Angeles, CA, 90095, USA

²Bioengineering Department, University of California, Los Angeles, CA, 90095, USA

³California NanoSystems Institute (CNSI), University of California, Los Angeles, CA, 90095, USA

⁴Physics & Astronomy Department, University of California, Los Angeles, CA, 90095, USA

*Correspondence to: ozcan@ucla.edu

Abstract

Terahertz waves offer numerous advantages for the nondestructive detection of hidden objects/defects in materials, as they can penetrate through most optically-opaque materials. However, existing terahertz inspection systems are restricted in their throughput and accuracy (especially for detecting small features) due to their limited speed and resolution. Furthermore, machine vision-based continuous sensing systems that use large-pixel-count imaging are generally bottlenecked due to their digital storage, data transmission and image processing requirements. Here, we report a diffractive processor that rapidly detects hidden defects/objects within a target sample using a single-pixel spectroscopic terahertz detector, without scanning the sample or forming/processing its image. This terahertz processor consists of passive diffractive layers that are optimized using deep learning to modify the spectrum of the terahertz radiation according to the absence/presence of hidden structures or defects. After its fabrication, the resulting diffractive processor all-optically probes the structural information of the sample volume and outputs a spectrum that directly indicates the presence or absence of hidden structures, not visible from outside. As a proof-of-concept, we trained a diffractive terahertz processor to sense hidden defects (including subwavelength features) inside test samples, and evaluated its performance by analyzing the detection sensitivity as a function of the size and position of the unknown defects. We validated its feasibility using a single-pixel terahertz time-domain spectroscopy setup and 3D-printed diffractive layers, successfully detecting hidden defects using pulsed terahertz illumination. This technique will be valuable for various applications, e.g., security screening, biomedical sensing, industrial quality control, anti-counterfeiting measures and cultural heritage protection.

Introduction

Inspecting hidden structures within materials or samples represents a critical requirement across various applications, such as security screening, industrial manufacturing and quality control, medicine, construction, and defense. Non-invasive detection systems based on terahertz technology offer unique opportunities for this purpose due to the ability of terahertz waves to penetrate through most optically-opaque materials and grasp the molecular fingerprint information of the sample through the rich spectral signatures of different materials in the terahertz band.¹⁻⁵ For example, terahertz time-domain spectroscopy (THz-TDS) systems have been extensively used in various non-destructive quality control applications since they can provide frequency-resolved and time-resolved responses of hidden objects.⁶⁻⁹ However, existing THz-TDS systems are single-pixel and require raster scanning to acquire the image of the hidden features, resulting in relatively low-speed/low-throughput systems. Nonlinear optical processes can also be utilized to convert the terahertz information of the illuminated sample to the near-infrared regime to visualize the hidden structural information of the sample through an optical camera without raster scanning.¹⁰⁻¹³ However, these imaging systems offer relatively low signal-to-noise ratio (SNR) levels and require bulky and expensive high-energy lasers to offer acceptable nonlinear conversion efficiencies. Alternatively, terahertz information of the illuminated sample can be encoded using spatial light modulators and the image data can be resolved using computational methods without raster scanning.¹⁴⁻¹⁸ However, the physical constraints of spatial light modulators operating at terahertz wavelengths limit the speed, and increase the size, cost, and complexity of these imaging systems. In addition to these, currently available terahertz focal-plane arrays based on field-effect transistors and microbolometers do not provide time-resolved and frequency-resolved image data, limiting the types of structural information that can be detected.^{19,20} Due to these limitations, the space-bandwidth products (SBPs) of existing terahertz imaging systems are orders of magnitude lower than their counterparts operating in the visible band, limiting the overall system throughput.

Apart from these limitations of existing terahertz imaging systems, the identification of hidden structural features in test volumes through the processing of large-pixel-count image data is, in general, bottlenecked and challenging to reach high throughputs needed in many applications (e.g., industrial quality control and security screening) due to the digital storage, data transmission and image processing/classification requirements that are demanding for continuous imaging and sensing systems.

Here, we present a diffractive processor (**Figure 1**) that can rapidly detect hidden defects or objects within a target sample volume using a single-pixel spectroscopic terahertz detector. Unlike traditional approaches that involve point-by-point scanning and digital reconstruction of the target sample volume using a computer, this single-pixel diffractive processor rapidly inspects the volume of the test sample illuminated with terahertz radiation, without the formation or digital processing of an image of the sample. Stated differently, rather than formulating the detection and classification of defects or hidden objects as part of a standard machine vision pipeline (i.e., image, digitize and then analyze using a computer), instead, we treat the detection system as a coherent diffractive processor of terahertz waves that can all-optically search for and classify undesired or unexpected sources of secondary waves generated by diffraction through hidden defects or structures. In this sense, the diffractive defect processor can be considered an all-optical sensor for

unexpected or hidden sources of secondary waves within a test volume, which are detected through a single-pixel spectroscopic detector. Our design is comprised of a series of diffractive layers, optimized to modify the spectrum of the terahertz radiation scattered from the test sample volume according to the absence or presence of hidden structures or defects. The diffractive layers are jointly optimized using deep learning, and contain tens of thousands of subwavelength phase features. Once their deep learning-based training is complete, the resulting diffractive layers are physically fabricated using 3D printing or additive manufacturing, which forms an optical neural network.²¹⁻³⁴ When the test object volume is illuminated with terahertz radiation, the scattered terahertz waves from the object volume are all-optically processed by the diffractive network and sampled by a single-pixel spectroscopic detector at the output aperture of the system. The measured spectrum reveals the existence of hidden defects/structures within the sample volume all-optically, without the need for raster scanning or any image reconstruction or processing steps. Since these target structures or defects of interest are hidden within a solid volume, traditional machine vision approaches that operate at visible wavelengths cannot provide an alternative approach for these tasks.

We demonstrated a proof-of-concept of this diffractive terahertz processor by detecting hidden defects in silicon samples, which were prepared by stacking two wafers; one wafer containing etched defects and the other wafer covering the defective regions. The diffractive layers were designed to introduce a differential variation in the peak spectral intensity near two predetermined terahertz wavelengths. This diffractive defect sensor was realized using a single-pixel THz-TDS system with a plasmonic nanoantenna-based source^{35,36} generating pulsed terahertz illumination and a plasmonic nanoantenna-based detector³⁷ sampling the terahertz spectrum at the output aperture. We numerically analyzed the performance of our diffractive defect sensor by evaluating its detection sensitivity as a function of the size and the position of the hidden defects within the detection field-of-view (FOV), also covering subwavelength feature sizes. We fabricated the optimized diffractive layers using a 3D printer and conducted experimental tests for hidden defect detection. Our experimental results on silicon wafers with various unknown defect sizes and positions showed a good agreement with our numerical analysis, successfully revealing the presence of unknown hidden defects.

Our reported approach offers distinct advantages compared to the existing terahertz imaging and sensing systems. First, the hidden defect detection is accomplished using a single-pixel spectroscopic detector, eliminating the need for a focal plane array or raster scanning, thus greatly simplifying and accelerating the defect detection process. Second, the diffractive layers we employ are passive optical components, enabling our diffractive processor to analyze the test object volume without requiring any external power source except for the terahertz illumination and single-pixel detector. Third, our all-optical end-to-end detection process negates the need for memory, data/image transmission or digital processing using e.g., a graphics processing unit (GPU), resulting in a high-throughput defect detection scheme.

Although the diffractive defect processors reported in this work were primarily designed for the terahertz band, the underlying concept and design approaches are also applicable for defect detection in other parts of the spectrum, including infrared, visible, and X-ray. These unique capabilities of performing computational sensing without a digital computer or the need for

creating a digital 3D image will inspire the development of new task-specific all-optical detection systems and smart sensors. These systems can find diverse applications, such as industrial manufacturing and quality control, material inspection, detection/classification of hidden objects, security screening, and anti-counterfeiting measures. The non-destructive and non-invasive nature of this technology platform also makes it a valuable tool for sensitive applications, e.g., cultural heritage preservation and biomedical sensing. We believe that this framework can deliver transformative advances in various fields, where defect detection and materials diagnosis are of utmost importance.

Results

Figure 1 illustrates the basic principles of the proof-of-concept for our single-pixel diffractive terahertz processor design. As depicted in **Fig. 1a**, a set of diffractive layers is positioned before the sample under test to provide structured broadband illumination within a given detection FOV, acting as an all-optical front-end network that is trainable. Another group of diffractive layers, positioned after the test sample, acts as the jointly-trained back-end network, which all-optically performs the detection of hidden defects inside the target sample by encoding the defect information into the power spectrum at the single-pixel output aperture. This output spectrum is measured at two predetermined wavelengths, λ_1 and λ_2 , producing the spectral intensity values $s(\lambda_1)$ and $s(\lambda_2)$ that yield a normalized detection score $s_{\text{det}} = \frac{s(\lambda_1)}{s(\lambda_1)+s(\lambda_2)}$ ($s_{\text{det}} \in (0,1)$); see **Fig.**

1b. By comparing s_{det} at the single-pixel output with a pre-selected threshold s_{th} , the defect inference is performed to predict the existence of hidden defects within the target sample volume, i.e., $s_{\text{det}} \geq s_{\text{th}}$ for a defect, while $s_{\text{det}} < s_{\text{th}}$ indicates no defect. As will be detailed later on, we selected an unbiased threshold of $s_{\text{th}} = 0.5$ in our numerical analysis and experimental validation and, therefore a simple differential decision rule of $s(\lambda_1) \geq s(\lambda_2)$ indicates the existence of hidden defects, and $s(\lambda_1) < s(\lambda_2)$ indicates a defect-free (negative) sample. More details about the forward physical model and the joint training of the front-end and back-end diffractive layers of **Fig. 1a** are provided in the Methods section.

To demonstrate the feasibility of our nondestructive diffractive defect detection framework, we designed a proof-of-concept single-pixel diffractive terahertz processor that can effectively detect pore-like hidden defects within silicon materials; these defects are not visible from the outside. Such a capability is highly sought after in numerous industrial applications due to its high prevalence and significance in determining e.g., the quality, reliability, and performance of manufactured parts/products. To achieve this capability, as depicted in **Fig. 2a**, we created test samples with hidden defects by forming a stack of two silicon wafers that are in close contact with each other, where the surface of one of the wafers contained defect structures fabricated using photolithography and etching (see Methods for details). The inspection FOV of each test object was chosen as 2×2 cm. As illustrated in **Fig. 2a**, an exemplary defect is located somewhere inside the detection FOV at the interface between the two wafers. **Supplementary Fig. S1** includes additional photographs of a silicon test sample, showcasing its structure across 3 cross-sectional planes: planes F and B for the front and back surfaces of the stacked wafers, respectively, and plane D for the contact interface of the two silicon wafers. Such hidden defects cannot be inspected

by visible or infrared cameras and would normally demand scanning imaging systems using terahertz wavelengths to form a digital image of the test object to visualize or detect potential defects using a computer.

To achieve all-optical detection of such hidden defects using our single-pixel diffractive terahertz processor, we empirically selected $\lambda_1 = 0.8$ mm and $\lambda_2 = 1.1$ mm, and accordingly optimized the architecture of the diffractive terahertz processor and its layers using deep learning (see the Methods section). Our single-pixel diffractive processor design consists of four diffractive layers, with two positioned before the target sample and two positioned after the target sample, i.e., forming the front-end and back-end diffractive processors, respectively. Each of these diffractive layers is spatially coded with the same number of diffractive features (100×100), each with a lateral size of $\sim 0.53\lambda_m$, where $\lambda_m = (\lambda_1 + \lambda_2) / 2 = 0.95$ mm. The layout of this diffractive design is provided in **Fig. 2b**.

Since our diffractive processor needs to effectively detect the hidden defects of unknown shapes and sizes that may appear *anywhere* in the target sample volume, we adopted a data-driven approach by simulating a total of 20,000 silicon test samples with hidden defects of varying sizes and shapes for training our diffractive processor model. The defects within these simulated test samples were set to be rectangular, with their lateral sizes (D_x and D_y) randomly generated within a range of 1 to 3 mm and a depth (D_z) randomly chosen between 0.23 and 0.27 mm. The positions of these defects (x_d , y_d) were also randomly set within the detection FOV. We also modeled a test sample that has no defects in our numerical simulations, which forms the negative sample in our training data. To avoid our diffractive model being trained with a heavy bias towards positive samples (i.e., test samples with defects), during the formation of our training dataset, we created 20,000 replicas of our defect-free sample and mixed them with the 20,000 samples with defects, such that the final training set had a balanced ratio of positive and negative samples. We also generated a blind testing set composed of 2,000 samples with various defects following the same approach; all these defective test samples were created using different combinations of parameters (D_x , D_y , D_z , x_d , y_d) that are uniquely different than any of those used by the training samples.

In the training of our diffractive designs, we used a focal cross-entropy loss; see the Methods section.³⁸ This type of loss function can effectively reduce the penalization from samples that can be easily classified, such as those containing large hidden defects, thereby providing better detection sensitivity for more challenging samples, such as those with smaller-sized hidden defects. Moreover, in the training loss function, we also incorporated a term to impose constraints on the energy distribution of the output power spectrum (see the Methods section). This loss term aimed to maximize the output diffraction efficiency at λ_1 and λ_2 , while minimizing it at other neighboring wavelengths, which helped us enhance the single-pixel SNR at the desired operational wavelengths (λ_1 and λ_2). This design choice reduced the single-pixel output at other wavelengths, increasing our designs' experimental robustness. Additional details regarding the training data generation and the loss function that we used can be found in the Methods section.

Figure 2c shows the resulting diffractive layers after the training was complete. We numerically tested this diffractive processor design using the testing set containing 2,000 defective samples that we generated without any overlap with the training defective samples, as well as a test sample

without any defects. By using an unbiased classification threshold of $s_{\text{th}} = 0.5$, we found that 89.62% of the defective test objects were successfully classified, and the defect-free test sample was also correctly identified. These results confirm that our diffractive model with $s_{\text{th}} = 0.5$ could achieve 100% specificity (false positive rate, $\text{FPR} = 0\%$), while possessing a high sensitivity (i.e., true positive rate, $\text{TPR} = 89.62\%$) to successfully detect various hidden defects with unknown combinations of shapes and locations, demonstrating its generalization for hidden defect detection. Optimization of the value of s_{th} based on the training or validation sets results in $s_{\text{th}} = 0.4989$, which further improves our blind detection sensitivity (TPR) to 90.48% for the defective test samples, while maintaining a specificity of 100%. However, the value of the threshold in this case ($s_{\text{th}} = 0.4989$) is very close to the output score of a defect-free sample (i.e., $s_{\text{det (negative)}} = 0.4988 < s_{\text{th}}$), and this can potentially introduce false positives under experimental errors. Therefore, to be resilient to experimental imperfections and suppress potential false positives, we selected an unbiased threshold of $s_{\text{th}} = 0.5$, where $s(\lambda_1) \geq s(\lambda_2)$ indicates the existence of hidden defects and $s(\lambda_1) < s(\lambda_2)$ indicates a defect-free sample.

To comprehensively evaluate the efficacy of our single-pixel diffractive defect detection framework with a decision threshold of $s_{\text{th}} = 0.5$, we performed an in-depth analysis of the performance of our diffractive processor. First, we evaluated the impact of the defect geometry on the detection performance by testing samples with rectangular defects of various dimensions (D_x , D_y , and D_z) located randomly within the detection FOV. For a given combination of D_x , D_y , and D_z , we simulated 100 test defective samples and obtained the corresponding detection sensitivity; see **Fig. 3a and b**. By separately scanning the values of D_x , D_y , and D_z , we summarized the resulting defect detection accuracies of our diffractive processor in **Fig. 3c-h**. We observe that, as the lateral size (D_x or D_y) of the hidden defect reduces, the detection sensitivity decreases considerably, regardless of D_z . For instance, for a relatively large defect of size $D_x = D_y = 3$ mm and $D_z = 0.3$ mm located randomly across the detection FOV, the detection sensitivity (i.e., TPR) of our diffractive processor is 100%, while it drops to 57% when both D_x and D_y reduce to 0.75 mm, which is subwavelength compared to λ_1 and λ_2 . Additionally, the overall detection performance also shows a degradation trend as the defect depth D_z is reduced. For example, for test samples with D_x and D_y in the range of [2.5, 3] mm, located randomly within the detection FOV, the detection sensitivity reaches $\sim 99.7\%$ when D_z is 0.3 mm, but drops to $\sim 81.2\%$ as D_z reduces to 0.15 mm, which is much smaller than λ_1 and λ_2 . These analyses further reveal that, for a given detection sensitivity threshold of, e.g., $\text{TPR} = 75\%$, our diffractive processor design can achieve accurate detection of hidden defects that are $D_x, D_y \geq \sim 1.25$ mm ($\sim 1.32\lambda_m$) and $D_z \geq \sim 0.21$ mm ($\sim 0.22\lambda_m$) within a FOV of 2×2 cm ($\sim 21\lambda_m \times 21\lambda_m$). It should be noted that subwavelength defects in general present SNR challenges for conventional imaging systems even if a diffraction-limited image were to be formed and acquired to be digitally processed.

We further evaluated the capabilities of our diffractive terahertz processor to detect subwavelength defects located at different positions across the detection FOV (see **Fig. 3i**). For this analysis, the entire detection FOV of 2×2 cm was divided into a series of concentric circles of equal radius, forming ring-like regions denoted as R1 to R6 from the center to the edges. For each one of these regions, we performed $n=100$ simulations of hidden defect detection, and in each simulation, a subwavelength hidden defect of size $D_x = D_y = 0.75$ mm and $D_z = 0.18$ mm was positioned at a

random location within the corresponding region; see **Fig. 3j**. We observed that, when the hidden defect randomly appears within R1 to R4 regions, the detection sensitivity is maintained at $\sim 100\%$, but it drops to $< 70\%$ when the hidden defect falls within R5 (TPR = 65%) and R6 (TPR = 20%). These results reveal an outstanding detection sensitivity in a circular region with a diameter of 1.6 cm ($\sim 16.84\lambda_m$) at the center of the detection FOV. Stated differently, compared to utilizing the entire detection FOV of 2×2 cm, if we slightly reduce this inspection FOV to a diameter of 1.6 cm, the detection performance of our diffractive design can be significantly improved, allowing successful detection of even smaller, subwavelength hidden defects of $D_x, D_y > \sim 0.75$ mm ($\sim 0.79\lambda_m$) and $D_z > \sim 0.18$ mm ($\sim 0.19\lambda_m$) with a sensitivity of TPR $> 79\%$.

Next, we performed an experimental validation of our diffractive design using a THz-TDS setup with a plasmonic photoconductive source and single-pixel detector; see **Fig. 4a**. The diffractive layers of the design were fabricated through 3D printing, and the photos of these fabricated diffractive layers are shown in **Fig. 4b**. After their fabrication, these layers were assembled and aligned with the test samples using a 3D-printed holder, forming a physical diffractive terahertz defect sensor that is integrated with a THz-TDS setup; see **Fig. 4c and d**. Ten different exemplary silicon test samples, with or without hidden defects, were prepared for this experimental testing, where the hidden structures of these samples at plane D are shown in **Fig. 5b**. Among these test samples, No. 1-9 contained a hidden defect that cannot be visibly seen as the defect is located at plane D (between the two wafers); these defects possess different sizes and shapes (defined by D_x, D_y and D_z). Importantly, the combinations of the parameters (D_x, D_y, D_z, x_d, y_d) for these test samples were never used in the training set, i.e., these 9 test samples containing defects were new to our trained diffractive model. Furthermore, the defect samples No. 8 and No. 9 had unique characteristics in their defect structures: the defect in test sample No. 8 is a rectangle of 1×5 mm, a shape never included in the training set; and the defect in test sample No. 9 is a 1×3 mm rectangle but rotated 45° , where such a rotation was never seen by the diffractive model in the training stage. The specific geometric parameters (D_x, D_y, D_z, x_d, y_d) of each test object are provided in **Fig. 5e**. The other test sample, i.e., sample No. 10, contains no defects, i.e., represents the negative test sample. During our experiments, each test sample was measured 5 times, producing output power spectra shown in **Fig. 5e** (solid lines), which are compared to their numerically generated counterparts using the trained forward model (dashed lines). Despite the 3D fabrication errors/imperfections, possible misalignments, and other sources of error in our experimental setup, there is a good agreement between our experimental results and the numerical predictions. However, the measured spectral curves shown in **Fig. 5e** exhibit some small shifts towards longer wavelengths. To improve our SNR and build experimental resilience for hidden defect detection, we averaged the 5 spectral measurements for each test object and used the peak spectral values at the resulting average spectrum for $s(\lambda_1)$ and $s(\lambda_2)$; see **Fig. 5c**. Since we chose an unbiased detection threshold of $s_{th} = 0.5$, the straight line of $s(\lambda_1) = s(\lambda_2)$ is used as the boundary for judging the presence or absence of defects: $s(\lambda_1) \geq s(\lambda_2)$ indicates the existence of hidden defects and $s(\lambda_1) < s(\lambda_2)$ indicates a defect-free sample. As shown in **Fig. 5c**, the spectral data points corresponding to test samples No. 1-9 all lie above this decision boundary, indicating that these samples were predicted by our diffractive processor to contain hidden defects, demonstrating successful detection (true positive decisions). Meanwhile, the spectral data point for sample No.

10, which is defect-free, fell on the other side of this decision boundary, also revealing a correct inference (a true negative decision).

Next, we explored the false positive rate of our diffractive defect processor and conducted new experiments with another defect-free (negative) test sample that was measured 10 times through repeated measurements. We formed 252 unique combinations of these 10 spectral measurements in groups of 5, and for each random combination of measurements, we averaged the 5 spectral measurements for the defect-free test object and used the peak spectral values at the resulting average spectrum for $s(\lambda_1)$ and $s(\lambda_2)$ – same as before. The results of this analysis are reported in **Fig. 5d**, where we observed an FPR of $\sim 10.7\%$ for an unbiased detection threshold of $s_{\text{th}} = 0.5$.

Discussion

We presented an all-optical, end-to-end diffractive processor for the rapid detection of hidden structures and demonstrated a proof-of-concept defect detection sensor based on this framework. The success of our experimental results and analyses confirmed the feasibility of our single-pixel diffractive terahertz processor using pulsed illumination to identify various hidden defects with unknown shapes and locations inside test sample volumes, with minimal false positives and without any image formation, acquisition or digital processing steps.

Different approaches can be explored to further enhance the performance of our defect detection sensor. To achieve a larger detection FOV, one will need to enlarge the diffractive layers so that the possible defect information can be effectively processed by the diffractive layers using a larger numerical aperture (NA). Additionally, the number of trainable diffractive layers in both the front-end and back-end optical networks can be increased to improve the approximation power of the diffractive network by creating a deeper diffractive processor.^{30,39} Furthermore, if the detection of defects with even smaller features is required, we can use shorter terahertz wavelengths, with accordingly smaller diffractive features fabricated as part of each diffractive layer.

In the demonstrated diffractive defect sensor, we utilized only two wavelength components at the output power spectra of the single-pixel detector to encode the defect information. It is also conceivable to train a diffractive defect processor that utilizes more wavelengths, encoding additional information regarding the hidden defects such as e.g., the size and material type of the defect, which may lead to more comprehensive defect detection and classification capabilities. To achieve spectral encoding of such defect information using more wavelengths, a larger number of trainable diffractive features per design would, in general, be required; this increase would be approximately proportional to the number of wavelengths used to encode independent channels of information.³⁴

While the presented single-pixel terahertz processor enabled high-throughput detection of defects with feature sizes that are subwavelength, the maximum thickness of the test sample that can be probed in transmission mode would be limited by the terahertz absorption or scattering inside the sample volume. For highly absorbing samples or samples with metal cores, for example, the proposed transmission system will present limitations to probe deeper into the test sample volume. However, this limitation is not specific to our diffractive processor design, and is in fact commonly

shared by all terahertz-based imaging and sensing systems. In case the terahertz transmission from certain test samples creates major SNR challenges due to terahertz absorption and/or scattering within the depths of the test sample, the presented diffractive defect processor designs can be modified to work in reflection mode so that a partial volume of the highly absorbing and/or reflecting test objects can be rapidly probed and analyzed by our single-pixel diffractive processor. In this reflection mode of operation, the whole deep learning-based training strategy outlined in this work will remain the same, except that between the test sample and the encoder diffractive network there will be a beam splitter (e.g., a mylar film) that communicates with an orthogonally placed diffractive decoder that will be jointly trained with the front-end diffractive encoder, following the architecture we reported earlier in our Results section. Through this reflection mode of the diffractive processor, one can extend the applications of our all-optical hidden defect sensor to partially probe and analyze highly absorbing and/or scattering test objects that would otherwise not transmit sufficient terahertz radiation.

One additional potential limitation of our framework is uncontrolled mechanical misalignments among the diffractive layers that constitute the diffractive encoder and decoder networks, as well as possible lateral/axial misalignments that might be observed between the diffractive layers and the test sample volume. As a mitigation strategy, diffractive designs can be “vaccinated” to such variations by modeling these random variations and misalignments during the optimization phase of the diffractive processor to build misalignment-resilient physical systems. It has been shown in our earlier works that the evolution of diffractive surfaces during the deep learning-based training of a diffractive network can be regularized and guided toward diffractive solutions that can maintain their inference accuracy despite mechanical misalignments.^{25,28,33} This misalignment-tolerant diffractive network training strategy models the layer-to-layer misalignments, e.g., translations in x , y and z , over random variables and introduces these errors as part of the forward optical model, inducing “vaccination” against such inaccuracies and/or mechanical variations. In addition to mechanical misalignments, the same training scheme can also be extended to mitigate the effects of other potential error sources e.g., fabrication inaccuracies, refractive index measurement errors and detection noise, improving the robustness of single-pixel defect detector devices.

Finally, we would like to emphasize that the presented design and the underlying concept can also be applied to other frequency bands of the electromagnetic spectrum, such as the infra-red^{40–42} and X-ray^{43–46}, for all-optical detection of hidden objects or defects. With its unique capabilities to rapidly and accurately inspect hidden objects and identify unknown defects hidden within materials, we believe that the presented single-pixel diffractive terahertz processor can be useful for a variety of applications, including industrial quality control, material inspection and security screening.

Methods

Numerical forward model of a single-pixel diffractive terahertz processor. Our forward model of the single-pixel diffractive terahertz processor consists of successive diffractive layers that are modeled as thin dielectric optical modulation elements of different thicknesses, where the i^{th}

feature on the k^{th} layer at a spatial location (x_i, y_i, z_k) represents a complex-valued transmission coefficient, t^k , which depends on the illumination wavelength (λ):

$$t^k(x_i, y_i, z_k, \lambda) = a^k(x_i, y_i, z_k, \lambda) \exp(j\phi^k(x_i, y_i, z_k, \lambda)) \quad (1),$$

where a and ϕ denote the amplitude and phase coefficients, respectively. The diffractive layers are connected to each other by free-space propagation, which is modeled through the Rayleigh-Sommerfeld diffraction equation^{21,24}, with an impulse response of $f_i^k(x, y, z, \lambda)$:

$$f_i^k(x, y, z, \lambda) = \frac{z - z_k}{r^2} \left(\frac{1}{2\pi r} + \frac{1}{j\lambda} \right) \exp\left(\frac{j2\pi r}{\lambda}\right) \quad (2),$$

where $r = \sqrt{(x - x_i)^2 + (y - y_i)^2 + (z - z_k)^2}$ and $j = \sqrt{-1}$. $f_i^k(x, y, z, \lambda)$ represents the complex-valued field at a spatial location (x, y, z) at a wavelength of λ , which can be viewed as a secondary wave generated from the source at (x_i, y_i, z_k) . Following the Huygens principle, each diffractive feature in a diffractive network can be modeled as the source of a secondary wave, as in Eq. (2). As a result, the optical field modulated by the i^{th} diffractive feature of the k^{th} layer ($k \geq 1$, treating the input object plane as the 0^{th} layer), $E^k(x_i, y_i, z_k, \lambda)$, can be written as:

$$E^k(x_i, y_i, z_k, \lambda) = t^k(x_i, y_i, z_k, \lambda) \cdot \sum_{m \in M} E^{k-1}(x_m, y_m, z_{k-1}, \lambda) \cdot f_m^{k-1}(x_i, y_i, z_k, \lambda) \quad (3),$$

where M and z_* denote the number of diffractive features on the $(k - 1)^{\text{th}}$ diffractive layer and the z location of the $*^{\text{th}}$ layer. The axial distances between the input/output aperture, diffractive layers and the object under test can be found in **Fig. 2b**.

The amplitude and phase components of the complex transmittance of the i^{th} feature of diffractive layer k , i.e., $a^k(x_i, y_i, z_k, \lambda)$ and $\phi^k(x_i, y_i, z_k, \lambda)$ in Eq. (1), are defined as a function of the material thickness, h_i^k , as follows:

$$a^k(x_i, y_i, z_k, \lambda) = \exp\left(-\frac{2\pi\kappa_d(\lambda)h_i^k}{\lambda}\right) \quad (4),$$

$$\phi^k(x_i, y_i, z_k, \lambda) = (n_d(\lambda) - n_{\text{air}}) \frac{2\pi h_i^k}{\lambda} \quad (5),$$

where the wavelength-dependent dispersion parameters $n_d(\lambda)$ and $\kappa_d(\lambda)$ are the refractive index and the extinction coefficient of the diffractive layer material corresponding to the real and imaginary parts of the complex-valued refractive index $\tilde{n}_d(\lambda)$, i.e., $\tilde{n}_d(\lambda) = n_d(\lambda) + j\kappa_d(\lambda)$. These dispersion parameters for the 3D-printing material used in this work were experimentally measured over a broad spectral range (see **Supplementary Fig. S2**). The thickness values of the diffractive features h_i^k represent the learnable parameters of our diffractive processor devices, which are composed of two parts, $h_{\text{trainable}}$ and h_{base} :

$$h = h_{\text{trainable}} + h_{\text{base}} \quad (6),$$

where $h_{\text{trainable}}$ denotes the learnable thickness parameters of each diffractive feature and is confined between 0 and $h_{\text{max}} = 0.8$ mm. The additional base thickness, h_{base} , is a constant, which is chosen as 0.6 mm to serve as the substrate support for the diffractive layers. To achieve the constraint applied to $h_{\text{trainable}}$, an associated latent trainable variable h_v was defined using:

$$h_{\text{trainable}} = \frac{h_{\text{max}}}{2} \cdot (\sin(h_v) + 1) \quad (7).$$

Note that before the training starts, h_v values of all the diffractive features were initialized as 0.

We calculated the propagation of the optical field inside the sample volume using:

$$\tilde{f}^k(x, y, z, \lambda) = \frac{z - z_s}{r^2} \left(\frac{1}{2\pi r} + \frac{1}{j\lambda} \right) \exp \left(-\frac{2\pi r}{\lambda} \left(\kappa_{\text{object}}(\lambda) - jn_{\text{object}}(\lambda) \right) \right) \quad (8),$$

where the wavelength-dependent parameters $n_{\text{object}}(\lambda)$ and $\kappa_{\text{object}}(\lambda)$ are the refractive index and the extinction coefficient of the object material. In this paper, since silicon wafers were used as the test objects, $n_{\text{object}}(\lambda)$ and $\kappa_{\text{object}}(\lambda)$ were set to 3.4174 and 0, respectively (disregarding the negligible material absorption of silicon at our wavelengths of interest). After calculating the impulse response of optical field propagation inside the object volume \tilde{f}^k , the resulting complex field is calculated using Eq. (3), except that the f^k is replaced by \tilde{f}^k used for the object material. When the propagating optical field encounters a defect inside the object, we model the defect as a tiny volume element with a certain size, which can also be considered as a thin optical modulation element. Due to the difference in the material properties between the defect and the object, the presence of the defect introduces additional amplitude and phase changes, which can be calculated in our forward model using the following formula:

$$a_{\text{defect}}(x_i, y_i, z_k, \lambda) = \exp \left(-\frac{2\pi h_{\text{defect}}}{\lambda} \left(\kappa_{\text{defect}}(\lambda) - \kappa_{\text{object}}(\lambda) \right) \right) \quad (9),$$

$$\phi_{\text{defect}}(x_i, y_i, z_k, \lambda) = (n_{\text{defect}}(\lambda) - n_{\text{object}}) \frac{2\pi h_{\text{defect}}}{\lambda} \quad (10),$$

where $n_{\text{defect}}(\lambda)$ and $\kappa_{\text{defect}}(\lambda)$ are the refractive index and the extinction coefficient of the object material, h_{defect} is the depth of the defect along the axial direction. In our experimental validation, these defects were fabricated by etching silicon wafers. Therefore, without loss of generality, air constitutes the material of the defects, i.e., $n_{\text{defect}}(\lambda) = n_{\text{air}}(\lambda) = 1$ and $\kappa_{\text{defect}}(\lambda) = \kappa_{\text{air}}(\lambda) = 0$.

Spectral scores for the detection of hidden objects and defects. Assuming that the diffractive design is composed of K layers (excluding the input, sample, and output planes), a single-pixel spectroscopic detector positioned at the output plane (denoted as the $(K + 1)^{\text{th}}$ layer) measures the power spectrum of the resulting optical field within the active area of the detector D , where the resulting spectral signal can be denoted as $s(\lambda)$:

$$s(\lambda) = \sum_{(x,y) \in D} |E^{K+1}(x, y, z_{K+1}, \lambda)|^2 \quad (11),$$

For the diffractive processor designs reported in this paper, the sizes of the detector active area and the output aperture are both set to be 2×2 mm. We sampled the spectral intensity of the diffractive network output at a pair of wavelengths λ_1 and λ_2 , resulting in spectral intensity values $s(\lambda_1)$ and $s(\lambda_2)$. The output detection score s_{det} of the diffractive processor is given by:

$$s_{\text{det}} = \frac{s(\lambda_1)}{s(\lambda_1) + s(\lambda_2)} \quad (12),$$

For an unbiased detection threshold of $s_{\text{th}} = 0.5$, this Eq. (12) boils down to a differential detection scheme where $s(\lambda_1) \geq s(\lambda_2)$ indicates the existence of hidden defects and $s(\lambda_1) < s(\lambda_2)$ indicates a defect-free sample. In this paper, λ_1 and λ_2 were empirically selected as 0.8 and 1.1 mm, respectively. To analyze the classification results produced by our diffractive processor design, we analyzed the numbers of true positive, false positive, true negative and false negative samples, denoted as n_{TP} , n_{FP} , n_{TN} and n_{FN} , respectively. Based on these, we reported the sensitivity (i.e., true positive rate, TPR), the specificity, the false negative rate (FNR) and the false positive rate (FPR) using:

$$\text{Sensitivity} = \text{TPR} = \frac{n_{TP}}{n_{TP} + n_{FN}} = 1 - \text{FNR} \quad (13),$$

$$\text{Specificity} = \frac{n_{TN}}{n_{TN} + n_{FP}} \quad (14),$$

$$\text{False positive rate (FPR)} = 1 - \text{Specificity} = \frac{n_{FP}}{n_{TN} + n_{FP}} \quad (15).$$

During the training of our diffractive terahertz processor model, we assumed that the optical field at the input aperture of the system has a flat spectral magnitude, i.e., the total power of the illumination beam at λ_1 and λ_2 is equal in our numerical simulations. However, the pulsed terahertz source employed in our experimental TDS setup contained a different spectral profile within the band of operation. To calibrate our diffractive processor system, we performed a normalization step for the experimentally measured output power spectra for all the test samples using a linear correction factor $\sigma(\lambda)$, which was obtained using:

$$\sigma(\lambda) = \frac{\frac{s_{\text{sim}}^{(r)}(\lambda_2)}{s_{\text{exp}}^{(r)}(\lambda'_2)} - \frac{s_{\text{sim}}^{(r)}(\lambda_1)}{s_{\text{exp}}^{(r)}(\lambda'_1)}}{\lambda'_2 - \lambda'_1} (\lambda - \lambda_1) + \frac{s_{\text{sim}}^{(r)}(\lambda_1)}{s_{\text{exp}}^{(r)}(\lambda'_1)} \quad (16),$$

where $s_{\text{exp}}^{(r)}(\lambda'_1)$ and $s_{\text{exp}}^{(r)}(\lambda'_2)$ represent the experimentally measured output spectral intensity values corresponding to the spectral peaks closest to λ_1 and λ_2 , respectively, using the defect-free sample as the test object after averaging multiple spectral measurements. $s_{\text{sim}}^{(r)}(\lambda_1)$ and $s_{\text{sim}}^{(r)}(\lambda_2)$ are the numerically computed counterparts of $s_{\text{exp}}^{(r)}(\lambda_1)$ and $s_{\text{exp}}^{(r)}(\lambda_2)$, respectively. Based on $\sigma(\lambda)$, we normalized the experimental spectral curves $s_{\text{exp}}(\lambda)$ as:

$$\hat{s}_{\text{exp}}(\lambda) = \sigma(\lambda)s_{\text{exp}}(\lambda) \quad (17).$$

By following this calibration/normalization routine outlined above, our diffractive model can be used under different forms of input broadband radiation, without overfitting to any experimental radiation source, which forms an important practical advantage of our framework. Moreover, even if the experimental system contains certain manufacturing errors and misalignments that result in a mismatch with the ideal forward physical model, the spectral intensity peaks $s_{\text{exp}}^{(r)}(\lambda'_1)$ and $s_{\text{exp}}^{(r)}(\lambda'_2)$ near the two wavelengths λ_1 and λ_2 can still be utilized as references for the calibration of the system. **Fig. 5e** illustrates the normalized experimental spectral intensity $\hat{s}_{\text{exp}}(\lambda)$ defined by Eq. (17) for different test samples, and their normalized peak spectral intensity values near λ_1 and λ_2 , i.e., $\hat{s}_{\text{exp}}(\lambda'_1)$ and $\hat{s}_{\text{exp}}(\lambda'_2)$, are reflected in **Fig. 5c**. The experimental differential spectral scores presented in **Fig. 5d** were computed based on Eq. (12) by replacing $s(\lambda_1)$ and $s(\lambda_2)$ with $\hat{s}_{\text{exp}}(\lambda'_1)$ and $\hat{s}_{\text{exp}}(\lambda'_2)$, respectively.

Fabrication of the test samples. The defects on the silicon wafers were fabricated through the following procedure. First, a SiO₂ layer was deposited on the silicon wafers using low-pressure chemical vapor deposition (LPCVD). Defect patterns were defined by photolithography, and the SiO₂ layer was etched in the defect regions using reactive-ion etching (RIE). After removing the remaining photoresist, defects in silicon wafers were formed through deep reactive-ion etching (DRIE) with the SiO₂ layer serving as the etch mask. Finally, the SiO₂ layer was removed through wet etching using a buffered oxide etchant (BOE). We measured the depth of the defect regions, D_z , with a Dektak 6M profilometer, which was ~ 0.25 mm for all the prepared test samples.

The diffractive layers were fabricated using a 3D printer (Form 3, Formlab). To assemble the printed diffractive layers and input objects, we employed a 3D-printed holder (Objet30 Pro, Stratasys) that was designed to ensure the proper placement of these components according to our numerical design.

Terahertz time-domain spectroscopy setup. A Ti:Sapphire laser was used to generate femtosecond optical pulses with a 78 MHz repetition rate at a center wavelength of 780 nm. The laser beam was split into two parts: one part was used to pump the terahertz source, a plasmonic photoconductive nano-antenna array^{35,36}, and the other part was used to probe the terahertz detector, a plasmonic photoconductive nano-antenna array³⁷ providing a high sensitivity and broad detection bandwidth. The terahertz radiation generated by the source was collimated and directed to the scanned sample using an off-axis parabolic mirror, as shown in **Fig. 4a**. The output signal from the terahertz detector was amplified with a transimpedance amplifier (Femto DHPCA-100) and detected with a lock-in amplifier (Zurich Instruments MFLI). By changing the temporal delay between the terahertz radiation and the laser probe beam incident on the terahertz detector, the time-domain signal was obtained. The corresponding spectrum was calculated by taking the Fourier transform of the time-domain signal, resulting in an SNR of 90 dB and an observable bandwidth of 5 THz for a time-domain signal span of 320 ps.

Supplementary Information: This file contains:

- **Training loss functions**

- Training details of the single-pixel diffractive terahertz processor
- Supplementary Figures S1-S2.

References

- (1) Kawase, K.; Ogawa, Y.; Watanabe, Y.; Inoue, H. Non-Destructive Terahertz Imaging of Illicit Drugs Using Spectral Fingerprints. *Opt. Express* **2003**, *11* (20), 2549–2554. <https://doi.org/10.1364/OE.11.002549>.
- (2) Zimdars, D.; White, J. S.; Stuk, G.; Chernovsky, A.; Fichter, G.; Williamson, S. Large Area Terahertz Imaging and Non-Destructive Evaluation Applications. *Insight - Non-Destr. Test. Cond. Monit.* **2006**, *48* (9), 537–539. <https://doi.org/10.1784/insi.2006.48.9.537>.
- (3) Fukasawa, R. Terahertz Imaging: Widespread Industrial Application in Non-Destructive Inspection and Chemical Analysis. *IEEE Trans. Terahertz Sci. Technol.* **2015**, *5* (6), 1121–1127.
- (4) Yu, L.; Hao, L.; Meiqiong, T.; Jiaoqi, H.; Wei, L.; Jinying, D.; Xueping, C.; Weiling, F.; Yang, Z. The Medical Application of Terahertz Technology in Non-Invasive Detection of Cells and Tissues: Opportunities and Challenges. *RSC Adv.* **2019**, *9* (17), 9354–9363. <https://doi.org/10.1039/C8RA10605C>.
- (5) Tao, Y. H.; Fitzgerald, A. J.; Wallace, V. P. Non-Contact, Non-Destructive Testing in Various Industrial Sectors with Terahertz Technology. *Sensors* **2020**, *20* (3), 712. <https://doi.org/10.3390/s20030712>.
- (6) Hangyo, M.; Tani, M.; Nagashima, T. Terahertz Time-Domain Spectroscopy of Solids: A Review. *Int. J. Infrared Millim. Waves* **2005**, *26* (12), 1661–1690. <https://doi.org/10.1007/s10762-005-0288-1>.
- (7) Stoik, C. D.; Bohn, M. J.; Blackshire, J. L. Nondestructive Evaluation of Aircraft Composites Using Transmissive Terahertz Time Domain Spectroscopy. *Opt. Express* **2008**, *16* (21), 17039–17051. <https://doi.org/10.1364/OE.16.017039>.
- (8) Park, S.-H.; Jang, J.-W.; Kim, H.-S. Non-Destructive Evaluation of the Hidden Voids in Integrated Circuit Packages Using Terahertz Time-Domain Spectroscopy. *J. Micromechanics Microengineering* **2015**, *25* (9), 095007. <https://doi.org/10.1088/0960-1317/25/9/095007>.
- (9) Markl, D.; Bawuah, P.; Ridgway, C.; van den Ban, S.; Goodwin, D. J.; Ketolainen, J.; Gane, P.; Peiponen, K.-E.; Zeitler, J. A. Fast and Non-Destructive Pore Structure Analysis Using Terahertz Time-Domain Spectroscopy. *Int. J. Pharm.* **2018**, *537* (1), 102–110. <https://doi.org/10.1016/j.ijpharm.2017.12.029>.
- (10) Wang, X.; Cui, Y.; Sun, W.; Ye, J.; Zhang, Y. Terahertz Real-Time Imaging with Balanced Electro-Optic Detection. *Opt. Commun.* **2010**, *283* (23), 4626–4632. <https://doi.org/10.1016/j.optcom.2010.07.010>.
- (11) Wang, X.; Cui, Y.; Sun, W.; Ye, J.; Zhang, Y. Terahertz Polarization Real-Time Imaging Based on Balanced Electro-Optic Detection. *JOSA A* **2010**, *27* (11), 2387–2393. <https://doi.org/10.1364/JOSAA.27.002387>.
- (12) Blanchard, F.; Tanaka, K. Improving Time and Space Resolution in Electro-Optic Sampling for near-Field Terahertz Imaging. *Opt. Lett.* **2016**, *41* (20), 4645–4648. <https://doi.org/10.1364/OL.41.004645>.

- (13) Usami, M.; Iwamoto, T.; Fukasawa, R.; Tani, M.; Watanabe, M.; Sakai, K. Development of a THz Spectroscopic Imaging System. *Phys. Med. Biol.* **2002**, *47* (21), 3749. <https://doi.org/10.1088/0031-9155/47/21/311>.
- (14) Shrekenhamer, D.; Watts, C. M.; Padilla, W. J. Terahertz Single Pixel Imaging with an Optically Controlled Dynamic Spatial Light Modulator. *Opt. Express* **2013**, *21* (10), 12507–12518. <https://doi.org/10.1364/OE.21.012507>.
- (15) Zhao, J.; E, Y.; Williams, K.; Zhang, X.-C.; Boyd, R. W. Spatial Sampling of Terahertz Fields with Sub-Wavelength Accuracy via Probe-Beam Encoding. *Light Sci. Appl.* **2019**, *8* (1), 55. <https://doi.org/10.1038/s41377-019-0166-6>.
- (16) Shang, Y.; Wang, X.; Sun, W.; Han, P.; Ye, J.; Feng, S.; Zhang, Y. Terahertz Image Reconstruction Based on Compressed Sensing and Inverse Fresnel Diffraction. *Opt. Express* **2019**, *27* (10), 14725–14735. <https://doi.org/10.1364/OE.27.014725>.
- (17) Stantchev, R. I.; Yu, X.; Blu, T.; Pickwell-MacPherson, E. Real-Time Terahertz Imaging with a Single-Pixel Detector. *Nat. Commun.* **2020**, *11* (1), 2535. <https://doi.org/10.1038/s41467-020-16370-x>.
- (18) Zanotto, L.; Piccoli, R.; Dong, J.; Caraffini, D.; Morandotti, R.; Razzari, L. Time-Domain Terahertz Compressive Imaging. *Opt. Express* **2020**, *28* (3), 3795–3802. <https://doi.org/10.1364/OE.384134>.
- (19) Ojefors, E.; Baktash, N.; Zhao, Y.; Hadi, R. A.; Sherry, H.; Pfeiffer, U. R. Terahertz Imaging Detectors in a 65-Nm CMOS SOI Technology. *2010 Proc. ESSCIRC* **2010**, 486–489. <https://doi.org/10.1109/ESSCIRC.2010.5619749>.
- (20) Nemoto, N.; Kanda, N.; Imai, R.; Konishi, K.; Miyoshi, M.; Kurashina, S.; Sasaki, T.; Oda, N.; Kuwata-Gonokami, M. High-Sensitivity and Broadband, Real-Time Terahertz Camera Incorporating a Micro-Bolometer Array With Resonant Cavity Structure. *IEEE Trans. Terahertz Sci. Technol.* **2016**, *6* (2), 175–182. <https://doi.org/10.1109/TTHZ.2015.2508010>.
- (21) Lin, X.; Rivenson, Y.; Yardimci, N. T.; Veli, M.; Luo, Y.; Jarrahi, M.; Ozcan, A. Supplementary Materials of All-Optical Machine Learning Using Diffractive Deep Neural Networks. *Science* **2018**, *361* (6406), 1004–1008. <https://doi.org/10.1126/science.aat8084>.
- (22) Luo, Y.; Mengü, D.; Yardimci, N. T.; Rivenson, Y.; Veli, M.; Jarrahi, M.; Ozcan, A. Design of Task-Specific Optical Systems Using Broadband Diffractive Neural Networks. *Light Sci. Appl.* **2019**, *8* (1), 1–14. <https://doi.org/10.1038/s41377-019-0223-1>.
- (23) Li, J.; Mengü, D.; Luo, Y.; Rivenson, Y.; Ozcan, A. Class-Specific Differential Detection in Diffractive Optical Neural Networks Improves Inference Accuracy. *Adv. Photonics* **2019**, *1* (4), 046001. <https://doi.org/10.1117/1.AP.1.4.046001>.
- (24) Mengü, D.; Luo, Y.; Rivenson, Y.; Ozcan, A. Analysis of Diffractive Optical Neural Networks and Their Integration With Electronic Neural Networks. *IEEE J. Sel. Top. Quantum Electron.* **2020**, *26* (1), 1–14. <https://doi.org/10.1109/JSTQE.2019.2921376>.
- (25) Mengü, D.; Zhao, Y.; Yardimci, N. T.; Rivenson, Y.; Jarrahi, M.; Ozcan, A. Misalignment Resilient Diffractive Optical Networks. *Nanophotonics* **2020**, *9* (13), 4207–4219. <https://doi.org/10.1515/nanoph-2020-0291>.
- (26) Veli, M.; Mengü, D.; Yardimci, N. T.; Luo, Y.; Li, J.; Rivenson, Y.; Jarrahi, M.; Ozcan, A. Terahertz Pulse Shaping Using Diffractive Surfaces. *Nat. Commun.* **2021**, *12* (1), 37. <https://doi.org/10.1038/s41467-020-20268-z>.
- (27) Rahman, M. S. S.; Li, J.; Mengü, D.; Rivenson, Y.; Ozcan, A. Ensemble Learning of Diffractive Optical Networks. *Light Sci. Appl.* **2021**, *10* (1), 14. <https://doi.org/10.1038/s41377-020-00446-w>.

- (28) Li, J.; Mengu, D.; Yardimci, N. T.; Luo, Y.; Li, X.; Veli, M.; Rivenson, Y.; Jarrahi, M.; Ozcan, A. Spectrally Encoded Single-Pixel Machine Vision Using Diffractive Networks. *Sci. Adv.* **2021**, *7* (13), eabd7690.
- (29) Mengu, D.; Rivenson, Y.; Ozcan, A. Scale-, Shift-, and Rotation-Invariant Diffractive Optical Networks. *ACS Photonics* **2021**, *8* (1), 324–334. <https://doi.org/10.1021/acsphotonics.0c01583>.
- (30) Kulce, O.; Mengu, D.; Rivenson, Y.; Ozcan, A. All-Optical Information-Processing Capacity of Diffractive Surfaces. *Light Sci. Appl.* **2021**, *10* (1), 25. <https://doi.org/10.1038/s41377-020-00439-9>.
- (31) Luo, Y.; Zhao, Y.; Li, J.; Çetintaş, E.; Rivenson, Y.; Jarrahi, M.; Ozcan, A. Computational Imaging without a Computer: Seeing through Random Diffusers at the Speed of Light. *eLight* **2022**, *2* (1), 4. <https://doi.org/10.1186/s43593-022-00012-4>.
- (32) Li, J.; Hung, Y.-C.; Kulce, O.; Mengu, D.; Ozcan, A. Polarization Multiplexed Diffractive Computing: All-Optical Implementation of a Group of Linear Transformations through a Polarization-Encoded Diffractive Network. *Light Sci. Appl.* **2022**, *11* (1), 153. <https://doi.org/10.1038/s41377-022-00849-x>.
- (33) Bai, B.; Luo, Y.; Gan, T.; Hu, J.; Li, Y.; Zhao, Y.; Mengu, D.; Jarrahi, M.; Ozcan, A. To Image, or Not to Image: Class-Specific Diffractive Cameras with All-Optical Erasure of Undesired Objects. *eLight* **2022**, *2* (1), 14. <https://doi.org/10.1186/s43593-022-00021-3>.
- (34) Li, J.; Gan, T.; Bai, B.; Luo, Y.; Jarrahi, M.; Ozcan, A. Massively Parallel Universal Linear Transformations Using a Wavelength-Multiplexed Diffractive Optical Network. *Adv. Photonics* **2023**, *5* (1), 016003. <https://doi.org/10.1117/1.AP.5.1.016003>.
- (35) Yardimci, N. T.; Yang, S.-H.; Berry, C. W.; Jarrahi, M. High-Power Terahertz Generation Using Large-Area Plasmonic Photoconductive Emitters. *IEEE Trans. Terahertz Sci. Technol.* **2015**, *5* (2), 223–229. <https://doi.org/10.1109/TTHZ.2015.2395417>.
- (36) Turan, D.; Corzo-Garcia, S. C.; Yardimci, N. T.; Castro-Camus, E.; Jarrahi, M. Impact of the Metal Adhesion Layer on the Radiation Power of Plasmonic Photoconductive Terahertz Sources. *J. Infrared Millim. Terahertz Waves* **2017**, *38* (12), 1448–1456. <https://doi.org/10.1007/s10762-017-0431-9>.
- (37) Yardimci, N. T.; Jarrahi, M. High Sensitivity Terahertz Detection through Large-Area Plasmonic Nano-Antenna Arrays. *Sci. Rep.* **2017**, *7* (1), 1–8. <https://doi.org/10.1038/srep42667>.
- (38) Lin, T.-Y.; Goyal, P.; Girshick, R.; He, K.; Dollar, P. Focal Loss for Dense Object Detection; 2017; pp 2980–2988.
- (39) Kulce, O.; Mengu, D.; Rivenson, Y.; Ozcan, A. All-Optical Synthesis of an Arbitrary Linear Transformation Using Diffractive Surfaces. *Light Sci. Appl.* **2021**, *10* (1), 196. <https://doi.org/10.1038/s41377-021-00623-5>.
- (40) WORKMAN, J. J. Review of Process and Non-Invasive Near-Infrared and Infrared Spectroscopy: 1993–1999. *Appl. Spectrosc. Rev.* **1999**, *34* (1–2), 1–89. <https://doi.org/10.1081/ASR-100100839>.
- (41) Manley, M. Near-Infrared Spectroscopy and Hyperspectral Imaging: Non-Destructive Analysis of Biological Materials. *Chem. Soc. Rev.* **2014**, *43* (24), 8200–8214. <https://doi.org/10.1039/C4CS00062E>.
- (42) Usamentiaga, R.; Venegas, P.; Guerediaga, J.; Vega, L.; Molleda, J.; Bulnes, F. G. Infrared Thermography for Temperature Measurement and Non-Destructive Testing. *Sensors* **2014**, *14* (7), 12305–12348. <https://doi.org/10.3390/s140712305>.

- (43) Hanke, R.; Fuchs, T.; Uhlmann, N. X-Ray Based Methods for Non-Destructive Testing and Material Characterization. *Nucl. Instrum. Methods Phys. Res. Sect. Accel. Spectrometers Detect. Assoc. Equip.* **2008**, *591* (1), 14–18. <https://doi.org/10.1016/j.nima.2008.03.016>.
- (44) Mooney, S. J.; Pridmore, T. P.; Helliwell, J.; Bennett, M. J. Developing X-Ray Computed Tomography to Non-Invasively Image 3-D Root Systems Architecture in Soil. *Plant Soil* **2012**, *352* (1), 1–22. <https://doi.org/10.1007/s11104-011-1039-9>.
- (45) Pietsch, P.; Wood, V. X-Ray Tomography for Lithium Ion Battery Research: A Practical Guide. *Annu. Rev. Mater. Res.* **2017**, *47* (1), 451–479. <https://doi.org/10.1146/annurev-matsci-070616-123957>.
- (46) Janssens, K.; Van der Snickt, G.; Vanmeert, F.; Legrand, S.; Nuyts, G.; Alfeld, M.; Monico, L.; Anaf, W.; De Nolf, W.; Vermeulen, M.; Verbeeck, J.; De Wael, K. Non-Invasive and Non-Destructive Examination of Artistic Pigments, Paints, and Paintings by Means of X-Ray Methods. In *Analytical Chemistry for Cultural Heritage*; Mazzeo, R., Ed.; Topics in Current Chemistry Collections; Springer International Publishing: Cham, 2017; pp 77–128. https://doi.org/10.1007/978-3-319-52804-5_3.
- (47) Kingma, D. P.; Ba, J. Adam: A Method for Stochastic Optimization. *ArXiv14126980 Cs* **2014**.

Figures

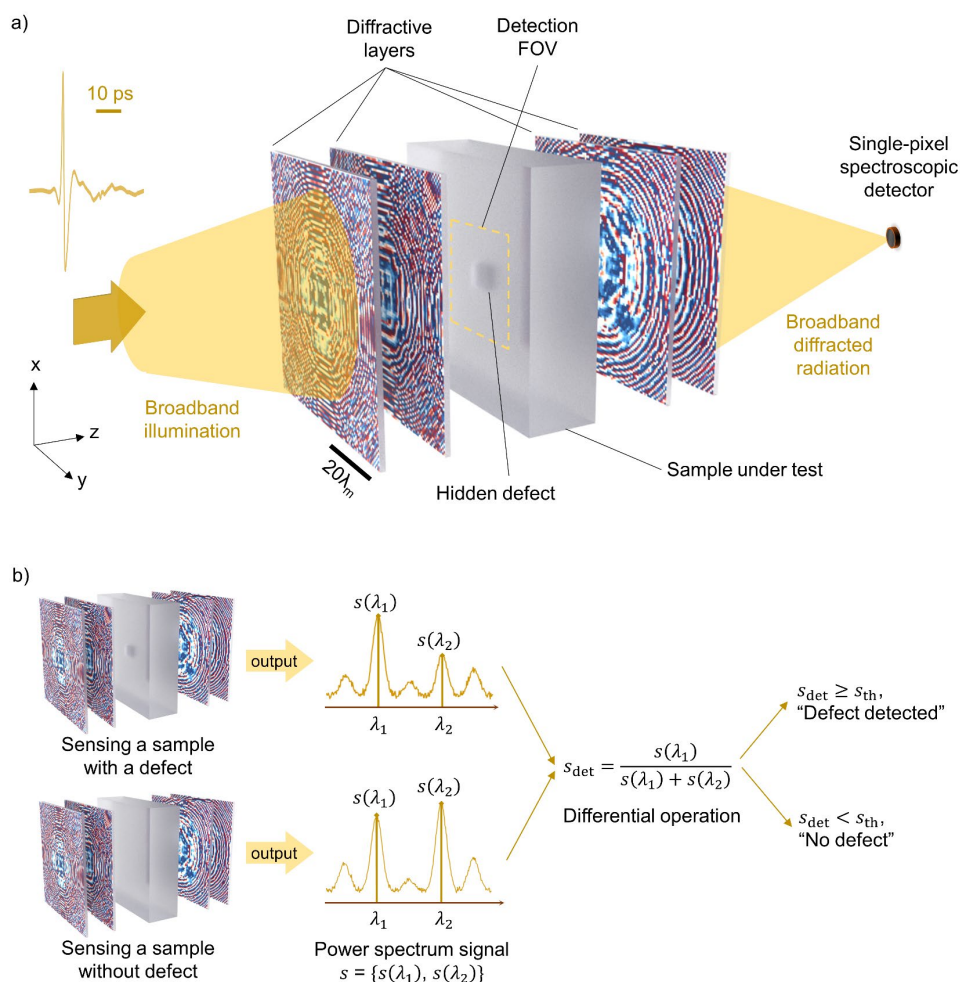


Figure 1. Schematic of a diffractive terahertz processor for rapid sensing of hidden objects or defects using a single pixel spectroscopic detector. **a**, Illustration of a single-pixel diffractive terahertz processor. The analysis and sensing of hidden defects are performed all-optically using passive and spatially-structured diffractive layers that encode the presence or absence of unknown defects hidden within the target sample volume into the output terahertz spectrum, which is then detected using a single-pixel spectroscopic detector. **b**, Working principle of the all-optical hidden object/defect detection scheme. The spectral intensity values, $s(\lambda_1)$ and $s(\lambda_2)$, sampled at two predetermined wavelengths λ_1 and λ_2 by the single-pixel detector are used to compute the output score for indicating the existence of hidden 3D defects/structures within the sample volume. $\lambda_m = (\lambda_1 + \lambda_2) / 2$.

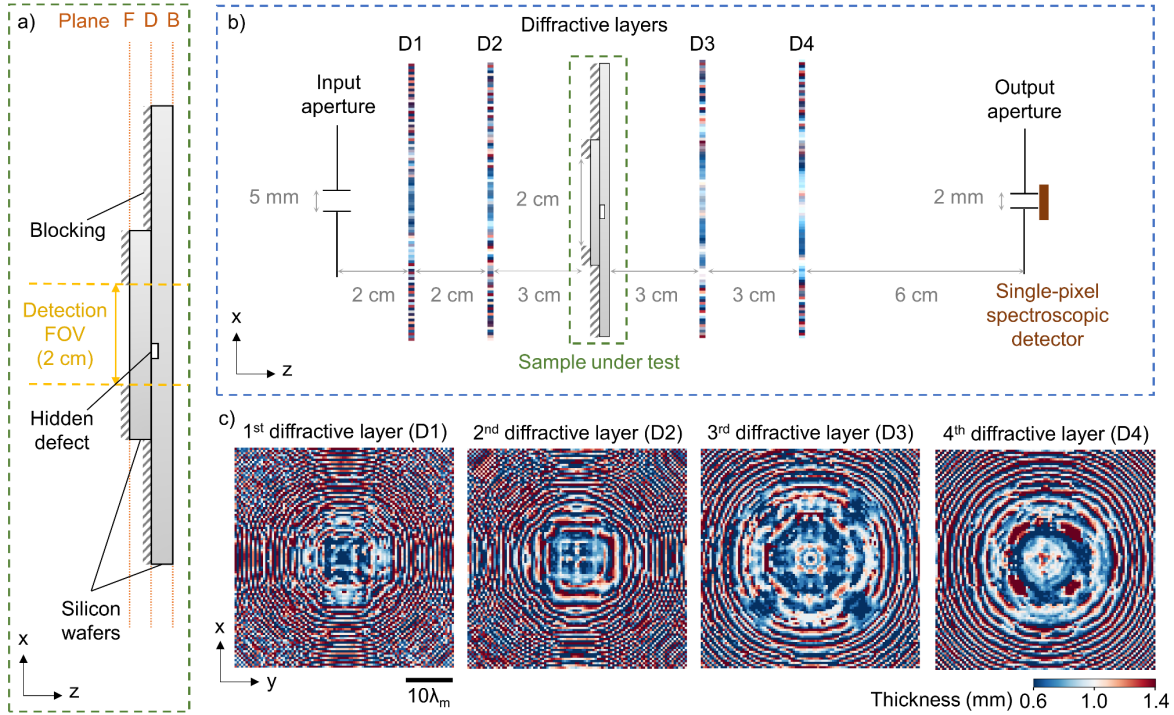


Figure 2. Design of the single-pixel diffractive terahertz processor for detecting hidden defects in silicon wafers. **a**, Side view schematic of the sample under test, comprising two silicon wafers stacked with a hidden defect structure fabricated on the surface of one of the wafers through photolithography and etching. The opaque regions are covered with aluminum to block the terahertz wave transmission, leaving a square-shaped opening of 2×2 cm that serves as the detection FOV. The photos showing cross-sections of a sample structure at planes F, D and B are provided in **Supplementary Fig. S1**. The direction of terahertz wave propagation is defined as the z direction, while the x and y directions represent the lateral directions. **b**, Physical layout of the single-pixel diffractive terahertz processor setup, with the sizes of input/output apertures, the size of the detection FOV, and the axial distances between the adjacent components annotated. **c**, Thickness profiles of the designed diffractive layers.

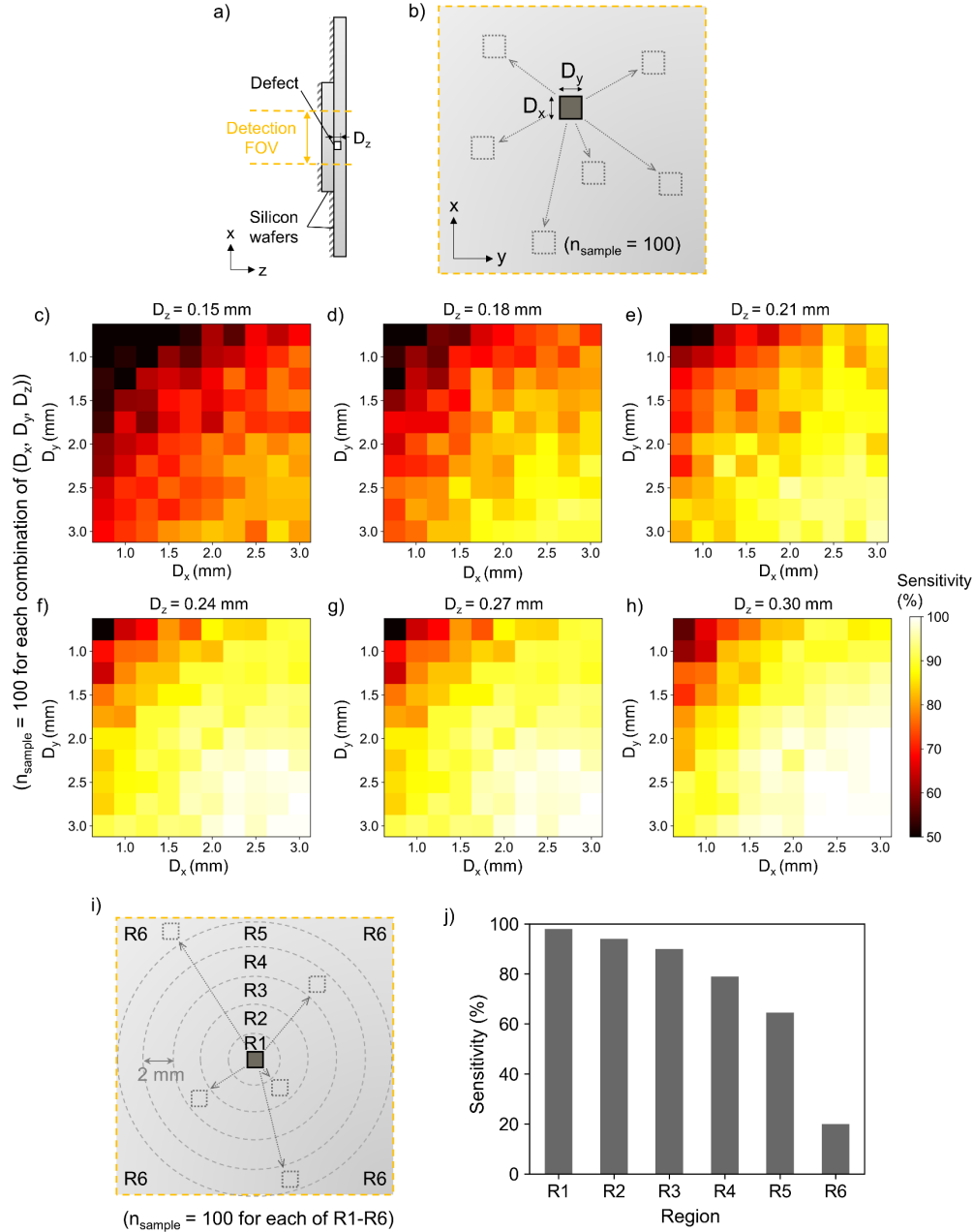


Figure 3. Performance analysis of the single-pixel diffractive terahertz processor design for detecting defects with different geometrical parameters and positions hidden inside the silicon test sample. a and b, Illustration for analyzing the impact of the shape and size of the hidden defect, defined by the lateral sizes, D_x and D_y , and the depth, D_z , on the detection sensitivity of the diffractive terahertz processor design. For a given combination of (D_x, D_y, D_z) , a total of $n_{\text{sample}} = 100$ test samples were numerically generated for each region (R1-R6), with each sample containing a hidden defect with a dimension of (D_x, D_y, D_z) located randomly across the detection FOV. **c-h,** Defect detection accuracies as a function of the defect dimensions (D_x, D_y and D_z) that are defined in (a) and (b). **i,** Illustration for analyzing the impact of the position of the hidden defect within the detection FOV on the detection sensitivity of the diffractive terahertz processor. For this analysis, the entire detection FOV is virtually divided into a series of concentric circles of equal

radius, forming ring-like regions, R1 to R6. For each of these regions, a total of $n_{\text{sample}} = 100$ test samples were numerically generated, each containing a hidden defect located randomly within the region. **j**, Resulting defect detection accuracies within different regions of the detection FOV that are defined in (i) using randomly located subwavelength hidden defects with $D_x = D_y = 0.75$ mm and $D_z = 0.18$ mm.

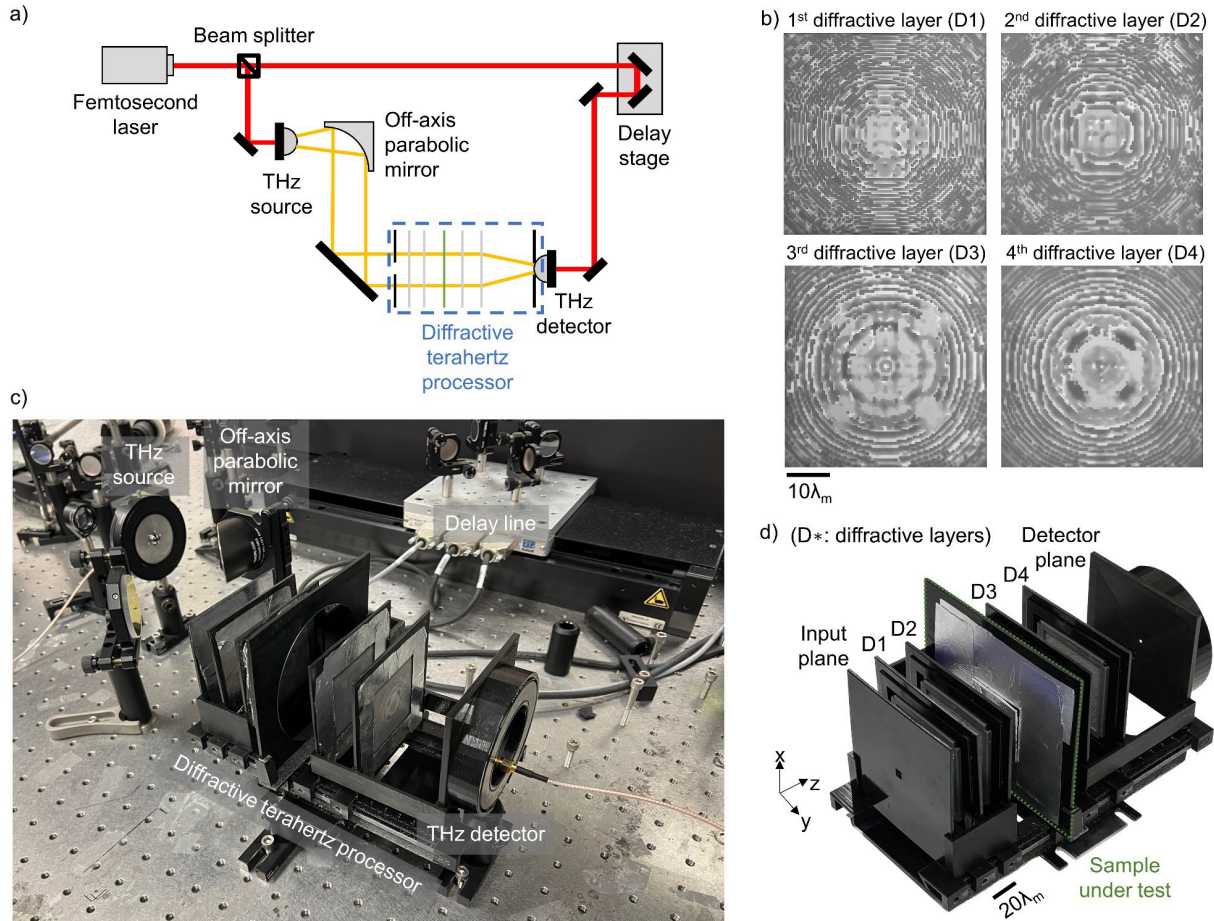


Figure 4. Experimental setup of the single-pixel diffractive terahertz processor. **a**, Schematic of the THz-TDS setup. Red lines represent the propagation path of the femtosecond pulses generated from a Ti:Sapphire laser operating at 780 nm to pump/probe the terahertz source/detector. Yellow lines depict the propagation path of the terahertz pulses, which are generated with a peak frequency of ~ 500 GHz and a bandwidth of ~ 5 THz and modulated by the 3D-printed diffractive terahertz processor to inspect the hidden structures within the test sample. **b**, Photographs of the 3D-printed diffractive layers. **c**, Photograph of the experimental setup. **d**, Photograph of the assembled diffractive terahertz processor. $\lambda_m = (\lambda_1 + \lambda_2) / 2 = 0.95$ mm.

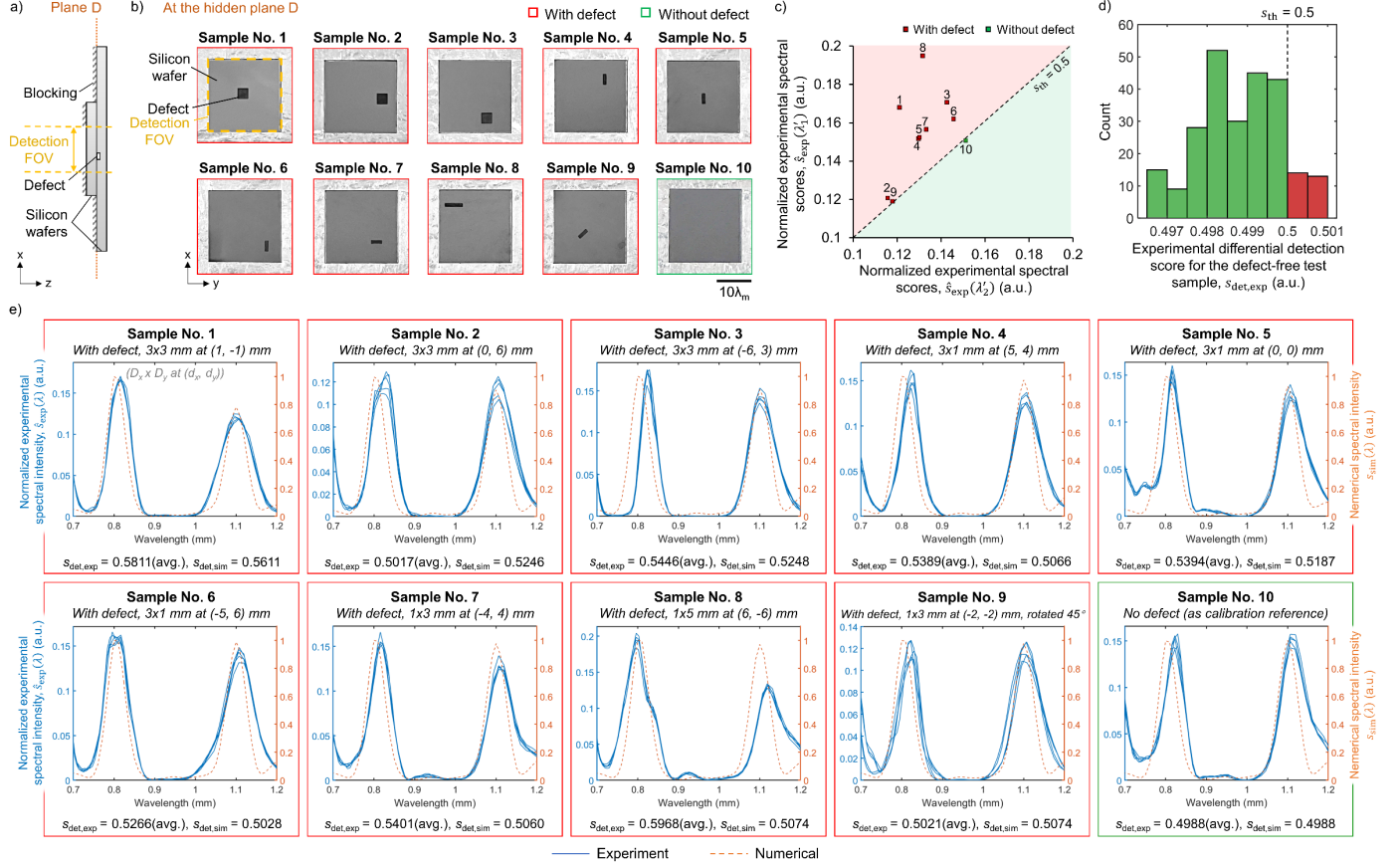


Figure 5. Experimental results for detecting defects hidden inside the test samples using the single-pixel diffractive terahertz processor. **a**, Illustration of the sample under test. **b**, Photographs of the exemplary test samples used for the experimental blind testing, which reveal the hidden structures at the cross-sectional plane D (not visible from outside). The first nine of the test samples (i.e., samples No. 1-9) contain etched defects that have different shapes and are positioned at different locations within the detection FOV, while the last sample (i.e., sample No. 10) has no defects. These photos were captured by removing the smaller silicon wafer at the front, i.e., the left wafer in (a). **c**, Normalized experimental spectral scores for the test samples shown in (b). **d**, Histogram showing the distribution of the 252 experimental differential detection scores, which were obtained through measuring a defect-free (negative) sample 10 times through repeated experiments and combining these 10 spectral measurements in unique groups of 5, each resulting in an experimental differential detection score, $s_{\text{det,exp}}$, based on the average spectrum. Note that $C \binom{10}{5} = 252$, where C refers to the combination operation. **e**, Normalized experimental spectral intensity (solid lines) for the different test samples shown in (b), compared with their numerically simulated counterparts (dashed lines). Each test sample was measured 5 times and the results of all 5 measurements are shown in the same graph. For the test samples with defects (i.e., samples No. 1-9), the lateral sizes (D_x and D_y) and positions (x_d , y_d) of the defects are shown in italicized texts, and $D_z = 0.25$ mm. The experimental differential detection scores, $s_{\text{det,exp}}$, are calculated for each test sample based on averaging the 5 spectral measurements, which are also compared with their numerical counterpart $s_{\text{det,sim}}$, reported at the bottom of each panel.